



Dielectric relaxation and small polaron hopping transport in sol-gel-derived NiCr₂O₄ spinel chromite

Muhammad Javed^{a,b,*}, Ayaz Arif Khan^a, Jamal Kazmi^c, Mohd Ambri Mohamed^c,
Muhammad Nasir Khan^d, Mubushar Hussain^d, Rehana Bilkees^a

^a Department of Physics, University of Azad Jammu & Kashmir, Muzaffarabad, 13100, Pakistan

^b Department of Physics, University of Kotli, Kotli, 11100, Pakistan

^c Institute of Microengineering and Nanoelectronics, Universiti Kebangsaan Malaysia, 43600, Bangi, Malaysia

^d Physics Division Pakistan Institute of Nuclear Science and Technology P.O. Nilore, Islamabad, 45650, Pakistan

ARTICLE INFO

Keywords:

Spinel
Dielectric
Complex impedance
AC conductivity
Hopping

ABSTRACT

Herein, we have synthesized NiCr₂O₄ chromite by the sol-gel auto-combustion route. The refined X-ray powder diffraction pattern confirmed the single-phase formation of the material, which crystallized in a cubic normal spinel structure with space group Fd3m. The complex impedance study indicated the existence of relaxation phenomenon and predicted the semiconducting nature of the material. The frequency-dependent Nyquist plot modeled by (R_{GB}C_{GB}) (R_GQ_G) equivalent circuit exhibited the effects of grain and grain boundary to the electrical response of the compound over the measured temperature range of 263 – 393 K. The experimental AC conductivity data followed Jonscher's double power-law behavior, and the frequency exponent profile suggested small polaron hopping as the most probable transport mechanism for the sample. The complex modulus analysis showed the non-Debye type behavior of the material. In contrast, the dielectric constant exhibited dispersion in the low-frequency regime with a large tangent loss directly related to temperature.

1. Introduction

In the last few decades, there has been a surge of interest in electro-ceramic spinel oxides which took prime importance in the telecommunication and electronic industry due to their novel electromagnetic characteristics. It makes them worthwhile for their potential applications in the high quality filters, phase shifters, radiofrequency circuits, isolators, optoelectronics, read/write heads for high-speed digital tapes, electrochemical technology, transformer cores, and other devices [1,2]. Recently, the chromium based spinel oxides with stoichiometric composition ACr₂O₄ (A = Mg, Co, Fe, Zn, Cu, Mn, Cd, etc.) have attracted considerable interest in research fields due to their fascinating electronic properties and potential applications as humidity sensors [3], solid oxide fuel cells (SOFC) [4], semiconductors [5], magnetic materials [6], high-temperature ceramics with prominent optical features [7], super hard materials [8], biocides, and corrosion inhibitors [9]. Among spinel chromites, nickel chromite (NiCr₂O₄) has drawn considerable attention due to its striking electronic and magneto-dielectric features [10]. NiCr₂O₄ has been widely used in gas sensors [5],

photo-catalysts [11], heat or light sensitive micromechanical devices [12], pigments [13], and supercapacitor energy storage devices [14].

In spinel oxides, the electronic motion becomes confined to small dimensions when the size is reduced, and the separation between the valence and conduction bands becomes comparable to or greater than the thermal energy (k_BT). As a result, the material starts exhibiting semiconducting properties. Additional confinement increases the energy gap further, and the material becomes an insulator. The electrical transport mechanism in spinel chromite is closely related to the synthesis route which consequently affects the structural and morphological features of the material. The external parameters, comprising temperature, frequency, pressure, and humidity, also influence the various characteristic features of the material. Setting suitable conditions and optimizing physical parameters determine the uniqueness of a material for device-based applications. In this regard, complex impedance spectroscopy (CIS) has been employed to investigate the role of microstructural components in charge conduction and relaxation mechanism of a spinel system [15]. The response from electro-active regions, such as bulk, interface, and electrode, is critical to analyze

* Corresponding author at: Department of Physics, University of Azad Jammu & Kashmir, Muzaffarabad, 13100, Pakistan.

E-mail address: javedbinyousuf@gmail.com (M. Javed).

the overall electrical behavior of materials. CIS resolves the contributions of grains (Gs), grain boundaries (GBs), and electrode effects independently. It helps to understand the underlying phenomenon for electrical conduction and polarization that optimizes the parameters for device application. Using this technique, complex electrical quantities, such as impedance, dielectric permittivity, modulus, and tangent loss as a function of frequency and temperature, are measured for both real and imaginary parts [16]. The frequency dispersion of these quantities, which depend upon the type of atoms on the octahedral and tetrahedral sites in the spinel structure, determines the nature of transport mechanisms and characteristic activation energies of materials.

Different methods, such as sol-gel wet chemical reaction method [17], hydrothermal treatment [13], co-precipitation technique [18], and standard solid-state reaction method [17] have been reported for the preparation of NiCr₂O₄ nanocrystals. The sol-gel auto-combustion route is preferred over other methods due to its cost-effectiveness, environmental friendliness, and control over size and shape with improved crystallinity. This method involves an exothermic process based on self-sustained and thermally induced anionic redox reaction of xerogel. The precursors comprise an aqueous solution of desired metal salts as oxidizers and organic complexant as reductant. This makes the sol-gel auto-combustion method a useful route to control the distribution of metal cations at the tetrahedral and octahedral sites of the spinel crystal lattice by suitable choice of the fuel which burns unwanted phase out of the compound [20,21].

In this work, we synthesized nickel chromite (NiCr₂O₄) nanocrystalline material via the sol-gel auto-combustion method and investigated its structure and morphology. The impedance analysis, electrical transport properties, electric modulus with long- and short-range conduction, and dielectric properties were examined by impedance spectroscopic techniques over different ranges of frequency and temperature.

2. Experimental

Nickel chromite (NiCr₂O₄) spinel oxide was prepared by the sol-gel auto-combustion method. High-purity precursors were used: nickel nitrate Ni(NO₃)₂·6H₂O, chromium nitrate Cr(NO₃)₃·9H₂O, and citric acid C₆H₈O₇. In a typical synthesis of NiCr₂O₄, the 0.5 M solution of Ni(NO₃)₂·6H₂O and 1 M solution of Cr(NO₃)₃·9H₂O were prepared separately in 25 ml deionized (DI) water. Both solutions were stirred continuously for 1 h to obtain homogenous mixture. The 5 M aqueous solution of citric acid was prepared in DI water and nitrate to citrate ratio was fixed at 1. The resulting citrate solution was dropped into the nitrate solution under continuous stirring, and neutralization of the solution was achieved by adding ammonium hydroxide (NH₄OH). The overall solution was evaporated by heating it on a hot plate at 100 °C under intensive stirring for about 1–3 hours. The solution turned into a highly viscous gel which was then transferred to a muffle furnace, where self-ignition was initiated at the experimental temperature of 300 °C. This step yielded a green fluffy and spongy powder which was further ground and calcined at 900 °C for 6 h. The calcined sample of NiCr₂O₄ was mixed with 5 wt.% polyvinyl alcohol solution which was used as a binder. The powder was pelletized into a circular disc with 13.5 mm diameter and 1.5 mm thickness under a uniaxial hydraulic pressure of 75 bar. Subsequently, the circular disc was sintered at 900 °C for 6 h and cooled to room temperature under a cooling rate of 5 °C per minute.

X-ray diffraction (XRD) analysis was carried out using a powder diffractometer (Rigaku DMAX-3A) with CuK α radiation at a wavelength of 1.54 Å to investigate the crystalline phase and various structural parameters of the prepared sample. The XRD patterns were scanned in a 2 θ range of 10° to 80° with a scanning step size of 0.05°. The morphology of the sample was explored by field-emission scanning electron microscopy (FESEM), and elemental composition was identified by energy-dispersive X-ray (EDX) analysis. The impedance, dielectric, and conductivity measurements of the prepared pellet were performed

using an Alpha-N impedance analyzer (Novocontrol Germany) with a sinusoidal input signal of amplitude 500 mV. The pellet was scanned over a frequency range of 70 – 2 × 10⁶ Hz and a temperature range of 263 – 393 K. The data were extracted through a WINDATA software programmed by a fully automated computer interface and analyzed by Zview software.

3. Results and discussion

3.1. Structural and microstructural study

Fig. 1 shows the refined XRD profile of nickel chromite calcined at 900 °C. The observed diffraction pattern was refined and analyzed using the FullProf Suite program [22]. In the refinement process, the peak shape was modeled using the pseudo-Voigt function, and the background mode was set as 12-coefficient Fourier cosine series. Lattice parameters, atomic positions, scale factors, zero correction, preferred crystallographic orientations, full width at half maximum (FWHM) parameters (U, V, and W), occupancy, and isotropic temperature factors were iterated. The quality of fit was judged by reliable factors, which include the weighted profile discrepancy factor (R_{WP}; %), Bragg discrepancy factor (R_B; %), expected weighted profile factor (R_{exp}), crystallographic factor (R_F), and goodness of fit (G; %). The refined pattern revealed that the sample crystallized as a face-centered cubic normal spinel with the Fd3m space group, in accordance with JCPDS file no. 89-6615. No secondary phase impurity, such as Cr₂O₃, Ni₂O, nor any other oxide of Ni and Cr, was found in the reflection patterns, which indicates the single-phase growth of the spinel structure of NiCr₂O₄. The built-in BondStr program estimated the bond lengths and angles in FullProf Suite software. The refined results were listed in Table 1. The average crystallite size of the prepared sample was calculated using the Debye–Scherrer (D-S) equation and further compared with the size deduced from the Williamson–Hall (W-H) equation. The former is expressed by the following relation [23]:

$$D = \frac{K\lambda}{\beta \cos\theta} \quad (1)$$

where D is the average crystallite size, K is particle shape factor whose value is 0.9, λ is the wavelength of CuK α radiation used (0.154 nm), β is the FWHM of the intensity peak, and θ is half of the Bragg reflection angle. From the above XRD spectra of NiCr₂O₄, the FWHM values of the prominent peaks were estimated, and the corresponding angles at which maximum intensity appeared were recorded. The D-S plot was drawn between $\cos\theta$ and $1/\beta$, and crystallite size (72.029 nm) was estimated from the fit of Eq. (1) as shown in Fig. 2(a).

Given the W-H equation [24], we obtained the following:

$$\beta \cos\theta = \frac{K\lambda}{D} + 4\epsilon \sin\theta \quad (2)$$

where ϵ refers to the micro-strain induced in the lattice; the other parameters have the usual meaning. The W-H plot was drawn by plotting the estimated values of $\beta \cos\theta$ for the same peak against $\sin\theta$ as shown in Fig. 2(b). By fitting Eq. (2) to this plot, the crystallite size and micro-strain were recorded as 69.74 nm and 3.7259×10^{-6} units, respectively. The difference in crystallite size values from the D-S and W-H plots was due to the incorporation of crystallite lattice strain in the W-H method, resulting from defects such as twinning, dislocation, distortion, and imperfection.

The refined crystal information file was used as an input to VESTA software to realize the unit cell and crystal lattice of the prepared ceramic spinel oxide as shown in Fig. 3. Unlike cubic ferrite materials that can adopt any mode of spinel structures, such as normal, inverse, or mixed, chromites always crystallize as normal-phase spinel structure. In the normal version of a spinel structure, trivalent Cr³⁺ is situated in all the octahedral 16(d) sites, whereas the tetrahedral 8(a) site is

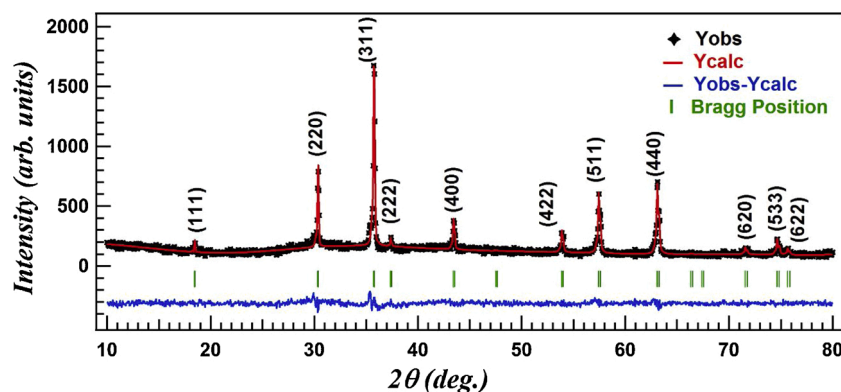


Fig. 1. Rietveld refined pattern of NiCr_2O_4 . Black symbols represent the experimental XRD pattern together with the calculated pattern (solid-red line), difference profile (blue line), and the standard Bragg positions (green vertical ticks).

Table 1

Structural and Rietveld refinement results of sol-gel auto-combustion-derived NiCr_2O_4 obtained from XRD powder diffraction data.

Crystal System	Space Group	Unit Cell Parameters (Å) $a = b = c$	Angles (°) $\alpha = \beta = \gamma$	Unit Cell Volume (Å ³)	Atomic Position					
Cubic (F)	Fd3m	8.330274	90	578.0665	Atom	Ox.	Site	X	y	z
Reliable Factors					Ni	+2	8a	0.3750	0.3750	0.3750
R _{wp}	R _{exp}	R _B	R _F	G	Cr	+3	16d	0.0000	0.0000	0.0000
12.33	9.9366	8.23	6.36	1.54	O	-2	32e	0.2392	0.2392	0.2392
BondStr Results										
Bond distance (Å)		Bond Angle (°)							Coordination	
Ni-O:	1.95982	O-Ni-O:	109.471,	Ni-O-O:	35.2644	O-Cr-O:	84.7078,		Ni-	4
Cr-O:	1.99643	Cr-O-O:	47.6461,	Ni-O-Cr:	121.600,	O-Cr-Ni:	28.9035,		Cr-	6
Cr-Cr:	2.94520	O-Ni-Cr:	29.4962,	Cr-O-Cr:	95.0573,	O-Cr-Cr:	42.4714		O:	
Crystallite size				Micro-strain						
D(D-S) nm		D(W-H) nm		3.7259×10^{-6}						
72.029		69.74								

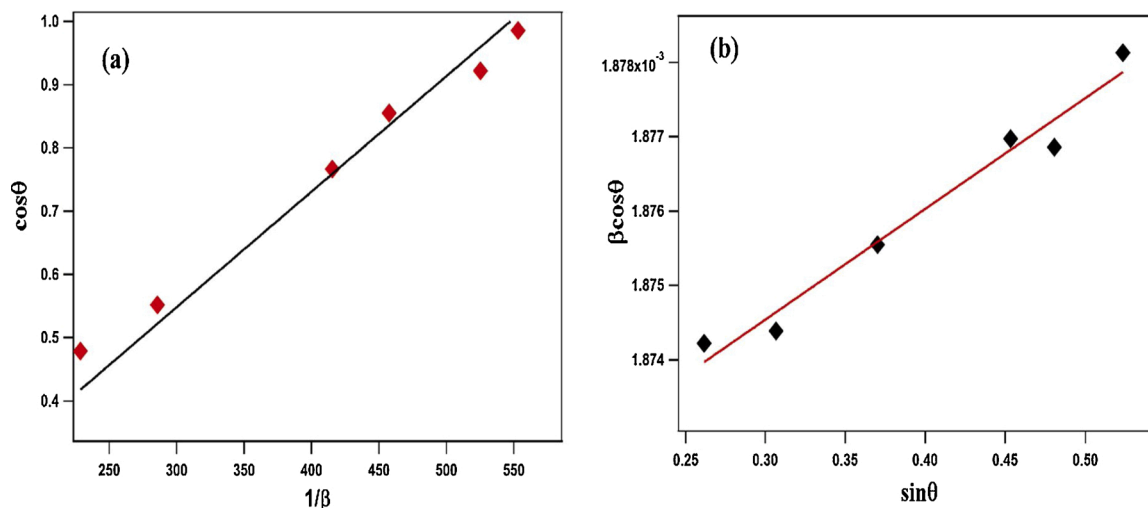


Fig. 2. (a) D-S and (b) W-H plots of NiCr_2O_4 annealed at 900 °C.

completely occupied by divalent metal Ni^{2+} . This condition is attributed to the large crystal field stabilization energy of chromium cations when situated in octahedral O^{2-} ligand coordination [25,26]. Fig. 3 reveals that the unit cell of $\text{NiO} \cdot \text{Cr}_2\text{O}_3$ with the normal spinel structure was built up with 8 formula units. This cubic spinel unit cell has 56 total atoms per unit cell, of which 32 are oxygen ions, and 24 are cations (Ni^{2+} and Cr^{3+}). The distribution of Cr^{3+} included 8 Cr^{3+} from the corner of the cube that contributed 1 Cr^{3+} to the unit cell and 12 Cr^{3+} from six faces (two for each center) of the cube that contributed 6 Cr^{3+} ions to the unit

cell. In contrast, five Cr^{3+} were contained completely within the unit cell. Thus, a total of $5 + 6 + 5 = 16$ Cr^{3+} ions existed per unit cell. On the other hand, 8 Ni^{2+} were present in the unit cell, with a total of $8 + 16 = 24$ metal cations per unit cell. However, 32 oxygen ions (O^{2-}) settled in a cubic closed packing and were accommodated on octahedral and tetrahedral sites with Cr and Ni ions, respectively (Fig. 3). Thus, the ratio of ions in the unit cell was $\text{Ni}^{2+}:\text{Cr}^{3+}:\text{O}^{2-} = 8:16:32 = 1:2:4$, which confirms the formula for the normal spinel structure of NiCr_2O_4 [18, 27–29].

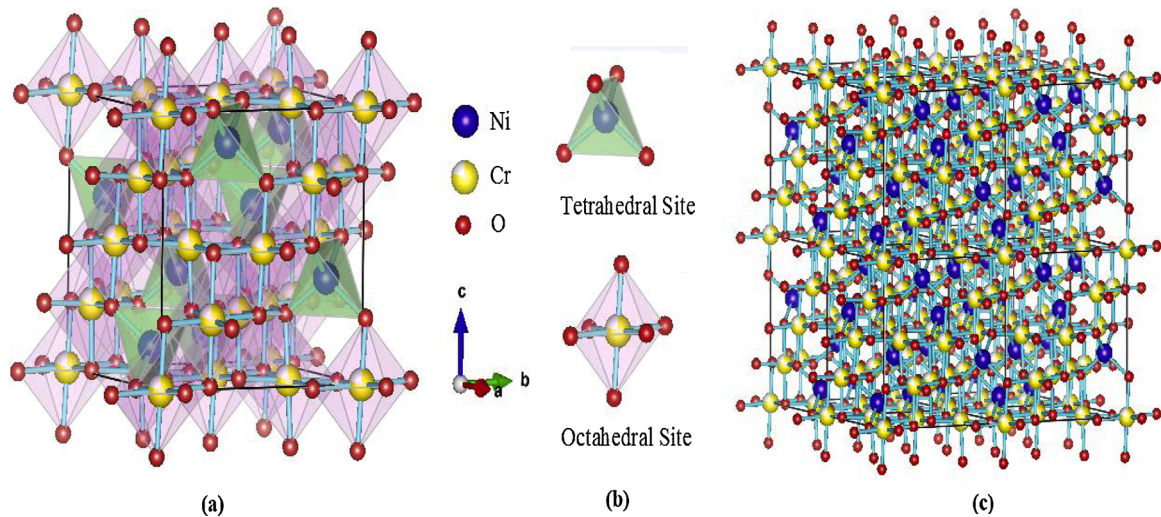


Fig. 3. (a) Unit cell, (b) NiO₄ tetrahedral and CrO₆ octahedral sites, and (c) crystal structure of NiCr₂O₄ normal spinel with space group Fd3m.

Fig. 4(a) and (b) shows the FESEM micrographs of NiCr₂O₄ spinel chromite calcined at 900 °C for 6 h with two different magnifications in micrometer and nanometer range, respectively. The micrograph structure reveals non-uniform Gs separated by distinctive GBs with no evident porosity. Fig. 4(c) shows the EDX profile of the sample; all elements were present with their atomic weight percent in accordance with the initial compositional stoichiometry. The results obtained from EDX analysis of NiCr₂O₄ spinel are in good agreement with those reported ones by Prabhulkar S. G. and Patil R. M [30]. Thus, the determination of elemental composition by EDX study confirmed the consistency of the Rietveld refinement model for the chromite under investigation.

3.2. Impedance analysis

Fig. 5(a) and (b) shows the temperature-dependent variations of the real part of impedance (Z') as a function of frequency over the temperature ranges of 263 – 328 K and 333 – 393 K (the insets depict a two-dimensional (2D) variation profile of Z' with frequency over the measured temperature ranges). The figure shows that a monotonous decrease in the values of Z' occurred with the increase in frequency and temperature. The variation patterns of Z' reveal the dispersion at low frequencies, followed by a plateau-type region. Finally, a merger appeared at all temperatures at which Z' became frequency-independent above a particular frequency value. This finding indicates that NiCr₂O₄ material possesses a negative temperature coefficient of resistance; its conduction should have an increasing trend with temperature and can thereby be declared to have a semiconducting behavior over the

concerning temperature range. At high frequencies, the merger of Z' marked the possible release of space charge at all temperatures. This effect is based on the reason that at sufficiently high frequencies, recombination occurs rapidly; thus, the space charge finds less time to relax, which resultantly reduces the space charge polarization, and the Z' curves merge at high frequencies [31,32].

Fig. 5(c) and (d) display the 3D plot of the imaginary part of impedance (Z'') against frequency over the experimental temperature limit from 263 to 328 and 333–393 K, respectively (the insets shows the 2D version of Z'' against frequency plot over the experimental temperature range). The complex impedance plot was used to explore significant features of the material, including the following: (i) a particular peak that appeared and was associated with relaxation frequency (f_{\max}) and Z'' that decreased monotonically with the further increase in frequency at all temperatures; (ii) the peak shifts toward higher frequencies with the decrease in the magnitude of Z'' and increase in temperature; (iii) the decreased height of the peak and broadening of width with temperature. The fall of the peak with temperature is based upon the perturbation caused by frequency in the network, which eases the charge carriers through the CrO₆ octahedral. As a result, Cr and O ions vibrate with a large amplitude, bring the carriers closer to each other, and results hopping between the sites. In this way, the frequency facilitates the crossing of charge carriers to the energy barriers, which contributes to the relaxation process of the material.

The relaxation time of the sample was measured with the peak location in accordance with the expression $\tau = \frac{1}{2\pi f_{\max}}$, where τ is the

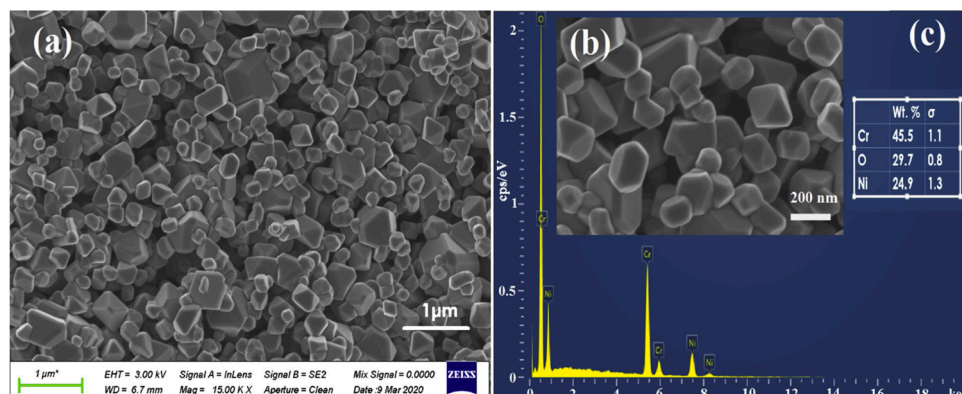


Fig. 4. Field-emission scanning electron micrographs with (a) low-magnification image, (b) high-magnification image, and (c) EDX spectrum of NiCr₂O₄.

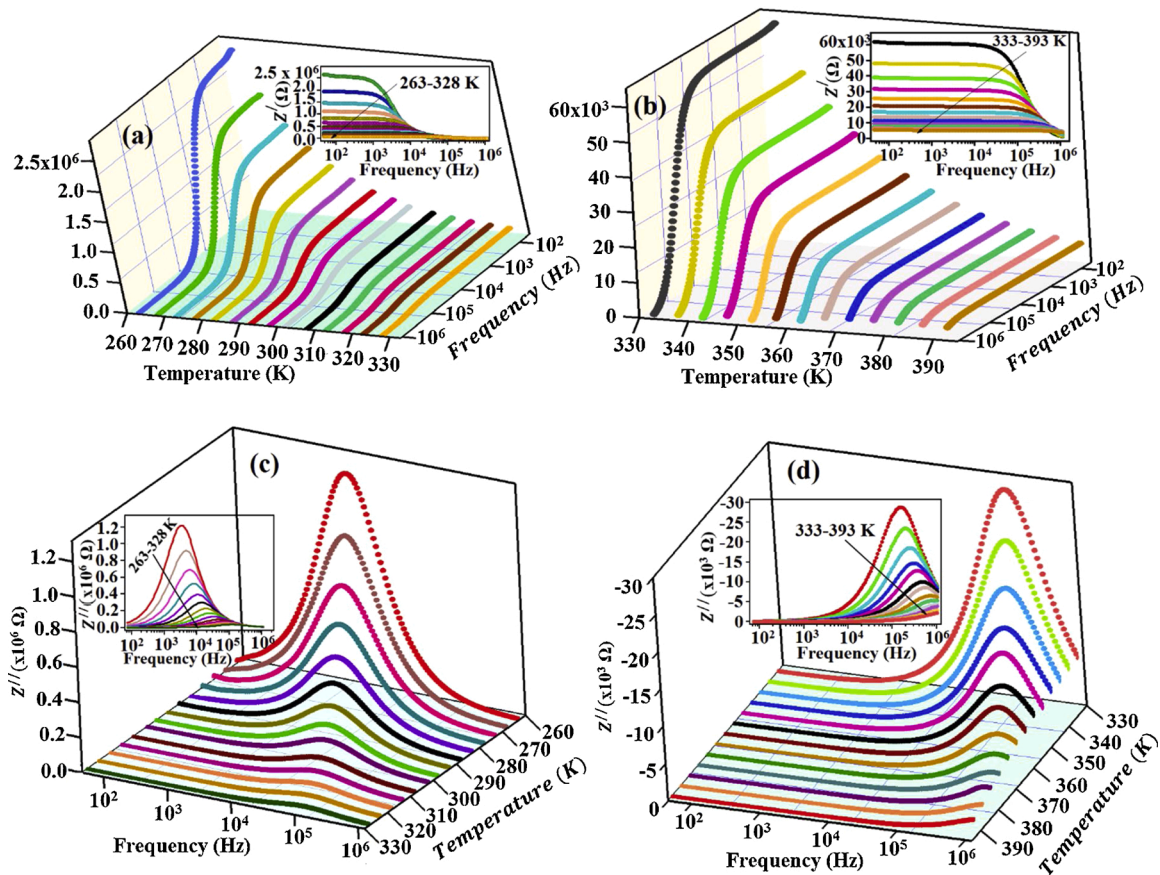


Fig. 5. Frequency-dependent variations of Z' and Z'' parts of complex electrical impedance of NiCr_2O_4 over the temperature ranges of 263–328 [(a) and (c)] and 333–393 K [(b) and (d)].

relaxation time, and f_{max} is the maximum frequency at which a peak appears. The log of relaxation time ($\ln\tau$) calculated from this relation was plotted with the inverse of temperature (T^{-1}) and showed a linear behavior (Fig. 6). This distribution of relaxation times is of Arrhenius nature, as expressed by the following relation:

$$\tau = \tau_0 \exp\left(\frac{E_a}{K_B T}\right) \quad (3)$$

where τ_0 designates the pre-exponential factor, K_B is Boltzmann constant, and E_a is the activation energy which was estimated after fitting the above Arrhenius relation to the plot and was found to be 185.040 ± 1.480 meV.

Fig. 7(a) and (b) shows the complex plane plots (Nyquist plots) of the impedance between Z' and Z'' parts for NiCr_2O_4 spinel over the measured temperature ranges of 263–328 and 333–393 K, respectively,

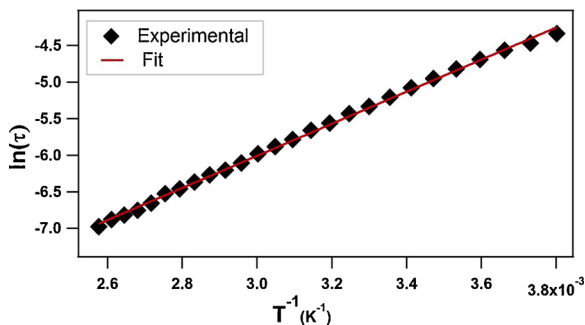


Fig. 6. Arrhenius plot of relaxation time distribution of NiCr_2O_4 with temperature.

with a temperature step size of 5 K for each range. The colored symbols demonstrate the actual experimental data, whereas the solid-black lines represent the fit administered by Zview software. In these plots, the frequency of the applied sinusoidal field increases from right to left side of the spectrum, and it was used to explore the most resistive parts in the sample [33]. Each curve comprises two depressed semi-circular arcs whose centers lie below the abscissa, which indicates the non-Debye type behavior and contribution of bulk and interface to the electrical characteristics of the material (inset of Fig. 7(a)). The diameter of the semicircle reached the maximum at 263 K, and it decreased with temperature, indicating the change in capacitive and resistive parts of the material and thermally activated process. Thus, the impedance of the material decreased with temperature.

An equivalent circuit model was proposed from the fit of experimental data to investigate the relationship between microstructure and electrical properties of the material. The model includes two parallel combinations designated as $(R_{GB}C_{GB})(R_GQ_G)$ shown as an inset in Fig. 7 (c), where R_{GB} , R_G , C_{GB} , and Q label the resistance of GBs, resistance of Gs, capacitance of GBs, and the constant phase element (CPE), respectively. In the Zview fitting procedure, Q accommodates heterogeneity in

the material, and the capacitance is estimated by $C = \left(R^{\frac{1-n}{n}}\right) Q^{\frac{1}{n}}$, where

the parameter n assumes the value unity for pure capacitance and zero for pure resistance. Fig. 7(c) shows the decreasing trend of electrical resistances of Gs and GBs with temperature. This finding marks the thermally activated mechanism and further suggests the semiconducting response of the material. These results are consistent with Z' and Z'' versus frequency plots. The resistance of GBs in NiCr_2O_4 has greater value than that of Gs at all temperatures. This condition may be due the

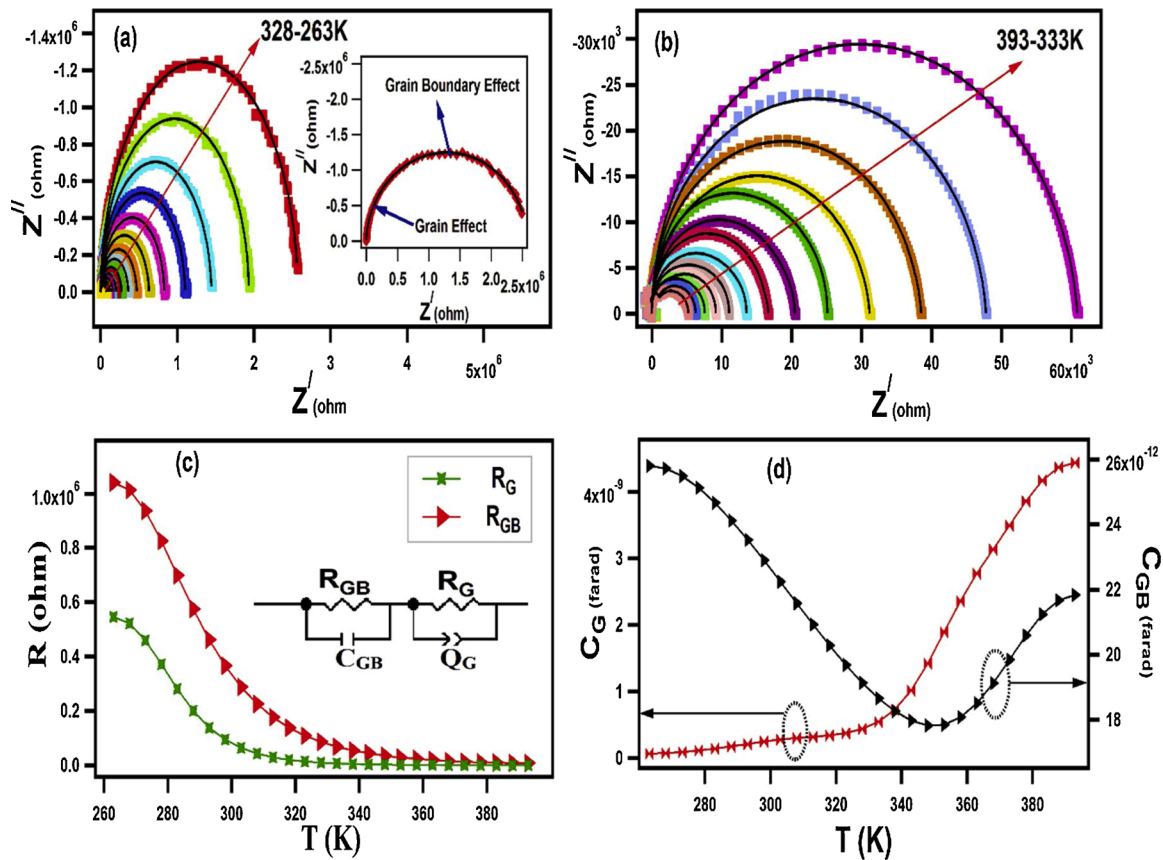


Fig. 7. (a), (b) Nyquist plots for NiCr₂O₄ modeled by the equivalent circuit in the temperature ranges of 263 – 328 and 333 – 393 K, respectively. (c) Variation in resistances of Gs and GBs with temperature and (d) temperature dependence of capacitances of Gs and GBs.

small concentration of defects and trapped charge carriers in the GBs. As a result, these boundaries provide minimal assistance to reduce the potential barriers to the mobility of charge carriers when activated compared with that of Gs. Such trends have been reported for other electro-ceramic materials [34]. Fig. 7(d) shows the temperature-dependent variation in capacitance of Gs (C_G) and GBs (C_{GB}). The values of C_G were of the order of 10^{-9} F (nF), whereas those of GBs (C_{GB}) were of the order of 10^{-12} F (pF). The higher C_G compared with C_{GB} can be due to the high concentration of defects, non-stoichiometric oxygen distribution, and canted spin alignment, which trapped the charge carriers, in Gs. The values of C_G increased with temperature, and this result may be due to the reduction in defect density with

temperature. On the other hand, the C_{GB} first decreased, reached a minimum value, and then increased with temperature. This trend is due to the thermal depopulation of the trapped charge carriers, which received adequate energy to cross over the boundary by hopping through the barrier height. However, with the further increase in temperature, the electronic and ionic charge density accumulation at the GBs increased, which resulted in an increased C_{GB} at higher temperatures [35].

The transport behavior of the NiCr₂O₄ material was investigated by applying the small polaron hopping (SPH) model to the data obtained from equivalent circuit modeling of complex plane plots. In the SPH mechanism, the resistance is expressed by the following relation [36]:

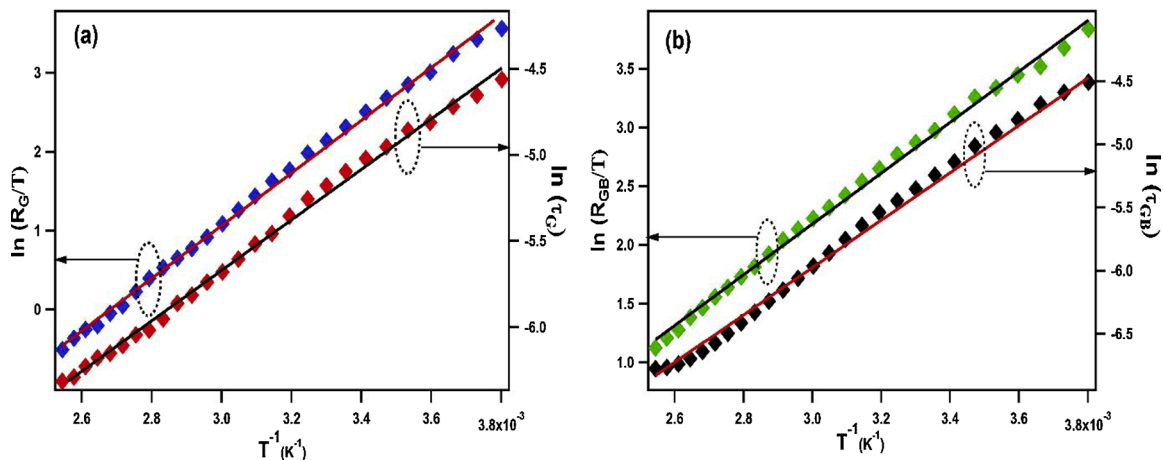


Fig. 8. Plots of (a) SPH model and (b) Arrhenius relations for relaxation times of Gs and GBs in NiCr₂O₄ material.

$$R = R_0 \text{Exp}\left(\frac{E_c}{K_B T}\right) \quad (4)$$

where R_0 is the pre-exponential factor, E_c is the activation energy of conduction phenomenon, K_B is Boltzmann constant, and T is the absolute temperature. Fig. 8(a) and (b) shows the fit of the SPH model given in Eq. (4) and Arrhenius fit of relaxation times for Gs and GBs, respectively. The figure reveals that the SPH model fits the experimental data well and is, therefore, a justified mechanism for electrical transportation in the material. The activation energies for conduction determined by SPH model fitting were 202.5 and 216.4 meV for Gs and GBs, respectively. The relaxation time was determined by the extracted values of resistances and capacitances of bulk and interface in accordance with the relation $\tau = RC$. The activation energy of relaxation phenomenon E_r was estimated by employing the Arrhenius relation: $\tau = \tau_0 \exp(E_r/K_B T)$. The activation energies for relaxation were 193.400 ± 1.241 meV and 203.500 ± 1.320 meV for Gs and GBs, respectively, and were approximately in close agreement with those obtained earlier from complex impedance against frequency spectra. The activation energies for conduction were slightly greater than those for relaxation mechanism because the conduction involved both the hopping energy and polaron binding energy, whereas the relaxation involved only the hopping energy [37].

3.3. Conductivity analysis

Fig. 9(a) and (b) shows the variations in AC electrical conductivity

(σ_{AC}) of NiCr_2O_4 material as a function of frequency in the temperature range 263–323 and 328–393 K, respectively. The conductivity pattern exhibited a typical behavior of ionic material, that is, it displayed a plateau-type response at low frequencies. The conductivity then increased sharply with the further increase in frequencies over the whole range of temperature measurements. In the low-frequency region up to 10^3 Hz, the conductivity was almost independent of frequency, which characterizes the DC part of conduction in the sample. The frequency at which the slope of conductivity was altered and above which the conduction involved the AC part of the conductivity is termed as the hopping frequency, which shifted towards higher frequencies with the rise in temperature. The dispersion of AC conductivity is generally characterized by Jonscher’s universal power-law, which expresses the transport mechanism based upon thermal activation of the hopping phenomenon between two sites with an energy barrier. According to this law, the total conductivity of a material is given by $\sigma(\omega) = \sigma_{DC} + A\omega^s$, where σ_{DC} is DC conductivity, A is a temperature-dependent pre-exponential factor, and s is a frequency exponent associated with the slope of the conductivity curve. The variation in exponent s with temperature characterizes the nature of the hopping mechanism in the materials. The direct variation in s with temperature determines the conduction by SPH [38], the inverse proportionality of s with temperature signifies the correlated barrier hopping mechanism [39], s decreases with temperature to attain the least value and then increases in the large polaronic hopping conduction [40], and if s sets itself fixed or close to 0.8, then the transport is governed by quantum mechanical tunneling in the material [41].

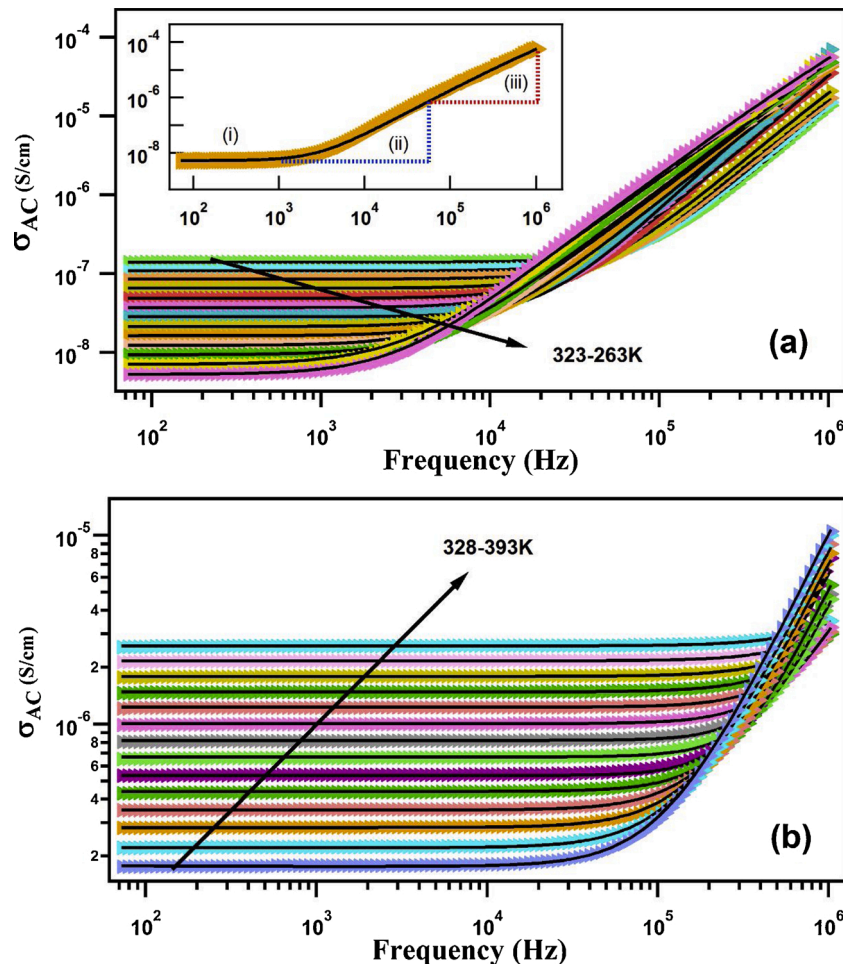


Fig. 9. Variation of AC conductivity as a function of frequency over various temperatures (a) from 263 – 323 (inset represents slopes of conductivity curve) and (b) 328 – 393 K.

In the current study, the conductivity spectrum of NiCr₂O₄ possessed three different regions corresponding to the contributions from various components of the material: (i) the conductivity below 10³ Hz infers the frequency-independent DC part of the conduction mechanism, (ii) the region from 10³ – 10⁵ Hz is attributed to the contribution from GBs; (iii) the third region above 10⁵ Hz marks the contribution from Gs as shown in the inset of Fig. 9(a). In such a situation, the total conductivity is expressed by Jonscher’s double power-law which is given by the following [42]:

$$\sigma_{AC} = \sigma_{DC} + A\omega^{s_1} + B\omega^{s_2} \tag{5}$$

where A and B are pre-exponential factors whose values depend on temperature and frequency, respectively. Herein, s₁ and s₂ are frequency exponents with values in the range 0 ≤ s₁ ≤ 1 and 1 ≤ s₂ ≤ 2, respectively. In Fig. 9, the symbols represent the experimental data of AC conductivity, and the solid- black lines reveal the fit by Jonscher’s double power-law expressed in Eq. (5).

The variation in DC conductivity with temperature followed the following Arrhenius expression:

$$\sigma_{dc} = \sigma_0 \exp\left(-\frac{E_a}{K_B T}\right) \tag{6}$$

where σ₀ is a pre-exponential factor, and E_a is the activation energy. By linear fitting of the expression in Eq. (6) to the plot in Fig. 10(a), the activation energy for DC conduction was measured as 187.340 ± 1.480 meV.

The values of s₁ and s₂ increased with temperature as shown in Fig. 10(b). The increasing pattern of s₁ and s₂ with temperature suggests that the SPH model governed the transport mechanism in NiCr₂O₄.

3.4. Electric modulus study

The study of complex electric modulus provides deep insights into the relaxation behavior of materials. It resolves the contribution from different parts of the system, such as bulk, interface, and electrode effects, on the transport mechanism. Fig. 11(a) shows the Cole–Cole plot of electric modulus between M'' and M' for NiCr₂O₄ chromite. The figure resolves two depressed semicircles in low- and high-frequency regions, inferring the contributions of GBs and Gs respectively, in the charge conduction and relaxation phenomenon at different temperatures. Moreover, each spectrum exhibited a zero value at the origin, which rules out the presence of electrode effect in the conduction mechanism of the material.

Fig. 11(b) shows the frequency dependence of the real part M' of the complex electric modulus of nickel chromite ceramic at several temperatures. The figure shows that M' possessed small, near-zero values in

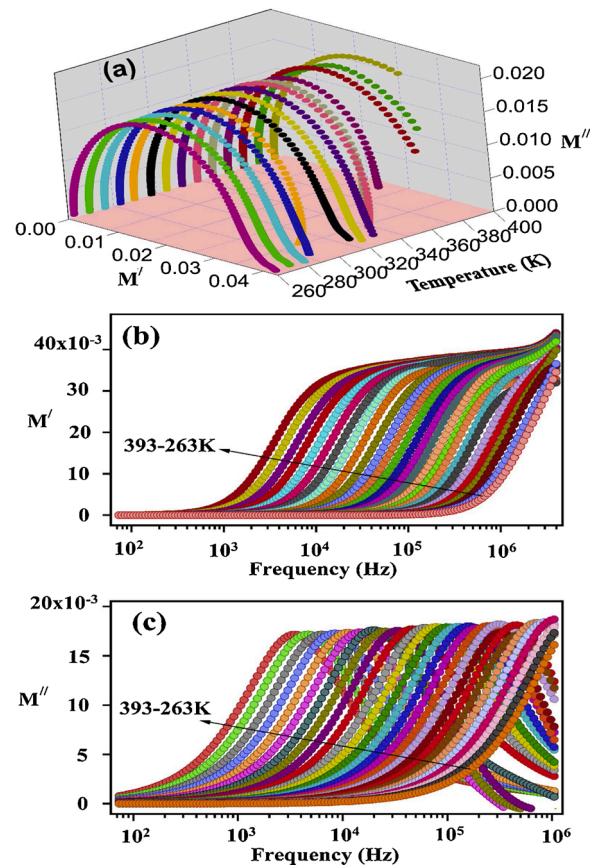


Fig. 11. (a) Cole–Cole plot and frequency dependence of (b) M' and (c) M'' parts of complex electrical modulus of NiCr₂O₄ spinel over the measured temperature range of 263–393 K.

the low-frequency region at all temperatures. This type of behavior is based on the negligible electrode polarization at low frequencies, which is due to the lack of the restoring force governing the mobility of charge carriers under an applied electric field [43]. The values of M' increased with the increase in frequency and finally reached the maxima M_∞ at high frequency, indicating the presence of relaxation processes in the material over the studied frequency range. The maximum value of M' decreased with the rise in temperature. In general, M' specifies the capability for energy storage of the sample. The reduction in maxima value with temperature is due to the increased mobility of charge carriers.

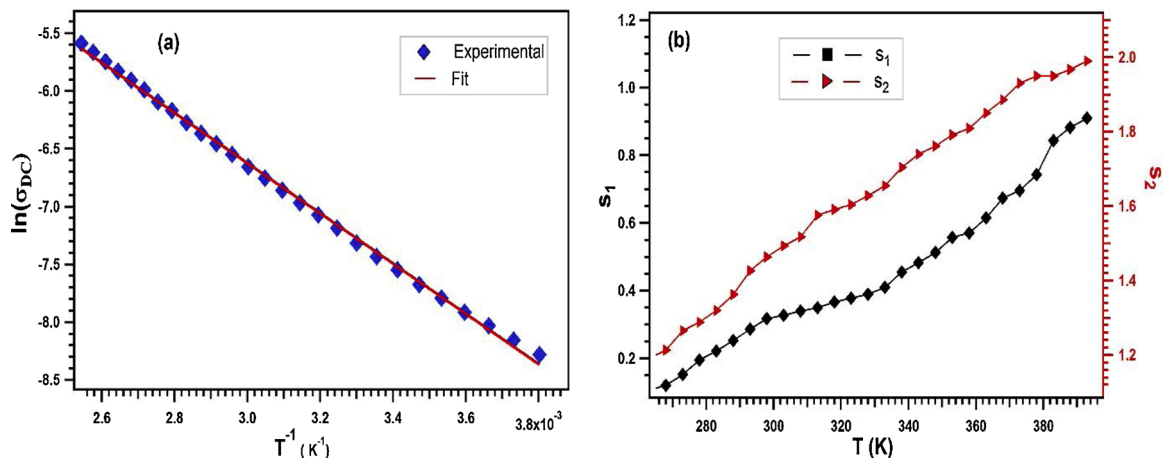


Fig. 10. (a) Variation in DC conductivity with the T⁻¹ and (b) temperature-dependent profile of frequency exponents s₁ and s₂.

Fig. 11(c) shows the variation in the imaginary part M'' of modulus against frequency over the experimental temperature range. The value of M'' increased with frequency, attained a maxima, and then declined with the further increase in frequency at all temperatures, which specifies the existence of thermal relaxation mechanism in the sample. The locus of peak maxima shifted toward higher frequencies, and the broadening of the peak increased with temperature. The asymmetry in the peak maxima determines the non-Debye type relaxation of the material. The frequency at which peak maxima M''_{max} occurred was designated as the f_M . The region below the f_M was attributed to the long-range mobility of charge carriers, whereas above the f_M , the charge carriers were confined and showed short-range mobility [44]. Fig. 12(a) shows the temperature-dependent variation of f_M which exhibited a linear pattern, and it can be manipulated by the Arrhenius relation with the following formula:

$$f_M = f_0 \exp\left(\frac{E_M}{K_B T}\right) \quad (7)$$

where f_0 is the pre-exponent factor, and E_M is the activation energy for relaxation. The activation energy calculated by the Arrhenius fit was 185.690 ± 1.881 meV. Thus, the activation energy estimated from the modulus profile is comparable to that obtained from impedance anal-

ysis. The comparable values of activation energies from both impedance and modulus suggest that the transport mechanism in NiCr₂O₄ material is governed by thermally activated hopping phenomena [45].

Fig. 12(b) illustrates the scaling behavior of the complex modulus of NiCr₂O₄ in the form of normalized plots between M''/M''_{max} and $\ln\left(\frac{f}{f_{max}}\right)$ at different temperatures. The low-frequency profile of the normalized peak in this modulus master curve infers the dynamics of charge carriers over long distances, whereas the high-frequency region of M''/M''_{max} versus $\ln\left(\frac{f}{f_{max}}\right)$ curve shows the spatial confinement of charge carriers to their potential wells, where they can exhibit localized motions. The region in which a peak appeared marks the transition from long- to short-range dynamics. The perfect merge of all the curves at all temperatures can be observed from the figure; this result suggests that the thermal energy remained the same for all possible relaxation mechanisms over various frequencies, and that the dynamical processes in the material are temperature independent; thus, the temperature change only altered the number of charge carriers and caused no change in the nature of overall conduction mechanism of the sample [46].

3.5. Dielectric permittivity analysis

Figs. 13(a) and 3 (b) shows the temperature dependence of the real

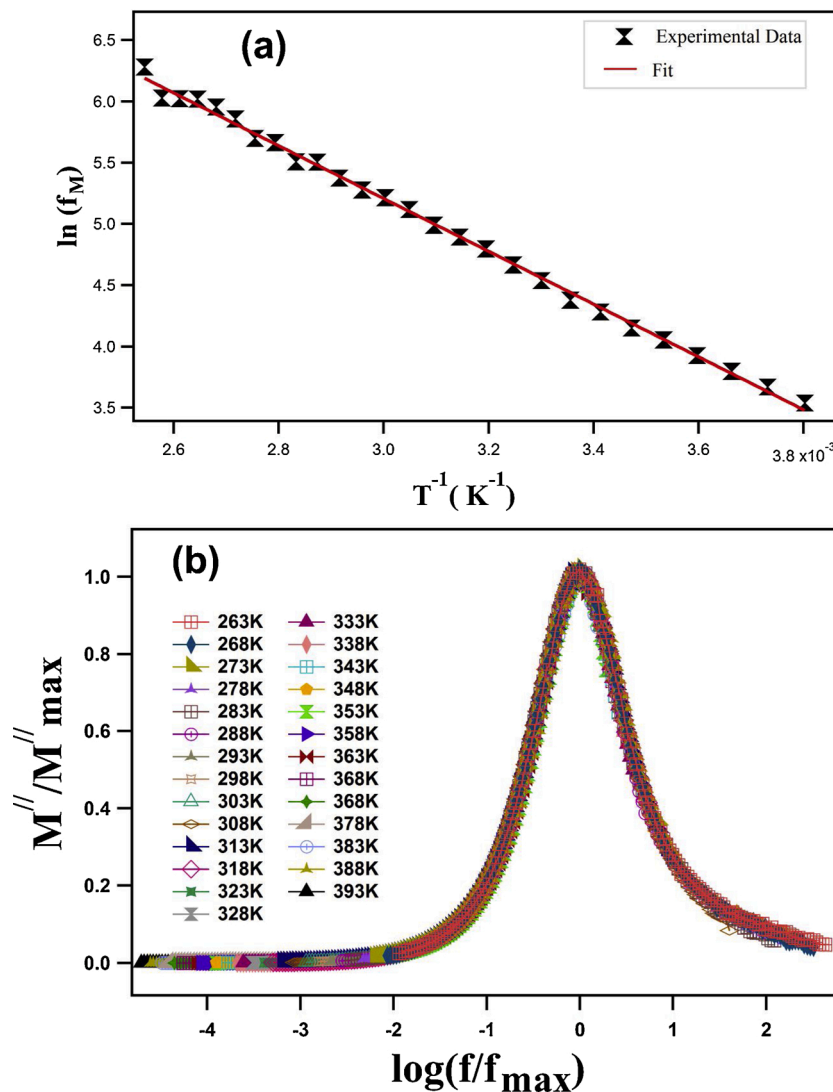


Fig. 12. (a) Arrhenius plot for relaxation frequencies with the T^{-1} and (b) normalized plots between M''/M''_{max} and $\ln\left(\frac{f}{f_{max}}\right)$ associated with complex electrical modulus.

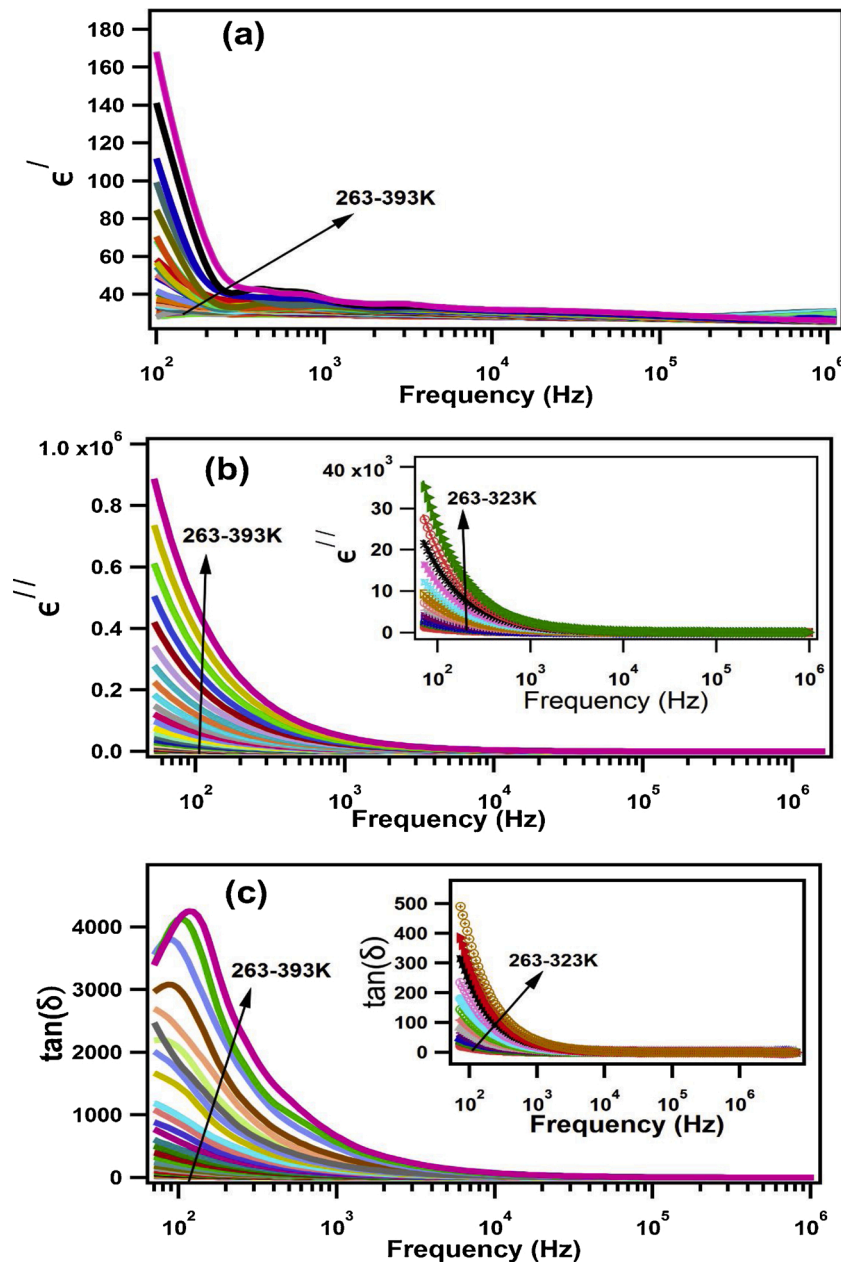


Fig. 13. Frequency-dependent variations in (a) ϵ' and (b) ϵ'' parts of dielectric and (c) dielectric loss at different temperatures.

(ϵ') and imaginary parts (ϵ'') of the dielectric constant, respectively, over different frequencies. The ϵ' deals with the energy storage of dielectric media through polarization, whereas the ϵ'' characterizes the energy loss of the material. The figure reveals that in the low-frequency region, the dielectric constant possessed high values for all temperatures. Moreover, the dielectric constant continually declined with frequency, because the increasing frequencies improved the mobility of the charge carriers which consequently decreased the dielectric constant. Furthermore, given the relaxation process, the electric dipoles cannot follow the field and lagged behind it. The magnitude of the dielectric constant increased directly with the temperature at a fixed frequency. This effect may be attributed to the nonalignment of dipoles in the direction of the field at low temperature. However, as the temperature increased, the dipoles obtained sufficient energy, and the thermal movements assisted the orientation of dipoles in the field direction. As a result, the magnitude of dielectric constant increased with temperature. Fig. 13(c) presents the dielectric loss ($\tan \delta$) = $\frac{Z''}{Z'}$ = $\frac{\epsilon''}{\epsilon'}$. At a constant

frequency, the dielectric loss increased with temperature. This trend can be inferred from the minimum loss in conduction at low temperatures; however, as the temperature increased, the loss in conduction also increased due to the enhanced conductivity; therefore, the value of dielectric loss was reinforced with the rise in temperature [47]. The behavior of $\tan \delta$ displayed dispersion in the low-frequency region and decreased with the increase in frequency, which implies that relaxation may be based upon thermal activation, and transport is directed by hopping mechanism as the peak loss is a fundamental factor for charge carriers in hopping conduction mechanism [48].

4. Conclusion

The sol-gel auto-combustion-derived nickel chromite annealed at 900 °C was crystallized in cubic spinel structure (NiCr_2O_4) with the Fd3m space group having Ni ions in tetrahedral and Cr ions in octahedral coordination with O ions. The temperature dependency of Z' with an inverse variation suggests a semiconducting behavior, whereas the

asymmetric broadening of the relaxation peak of Z'' implies the non-Debye nature of the material. The impedance complex plane plot exhibited two overlapping semicircles with $(R_{GB}C_{GB})(R_GQ_G)$ equivalent circuit modeling. The temperature-dependent AC conductivity followed Jonscher's double power-law and suggested hopping as a transport mechanism, as supported by the small polaron conduction model. The activation energy for conduction estimated by the Arrhenius relation showed a close agreement with those for the relaxation processes. The Cole-Cole plot of the modulus study indicated the contribution from Gs and GBs and identified the absence of electrode effects in the sample. The imaginary modulus M'' with long-tail approaching zero in the low-frequency side characterized the capacitive nature of the material and differentiated the long- and short-range mobility of the charge carriers. The shifting in the peak of M'' to a high frequency with temperature justified the presence of thermally activated phenomenon in the sample. The dielectric constant exhibited a decreasing trend with temperature, whereas the dielectric loss increased with the rise in temperature, which signifies the aligning trend of dipoles in the field direction with temperature.

Authorship contributions

The specific contributions made by each author is indicated by the surname. The name of each author must appear at least once in each of the three categories below.

Declaration of Competing Interest

The authors report no declarations of interest.

Acknowledgement

This work was supported in part by Universiti Kebangsaan Malaysia (The National University of Malaysia) grant no. GUP-2020-072.

References

- M.T. Rahman, M. Vargas, C.V. Ramana, Structural characteristics, electrical conduction and dielectric properties of gadolinium substituted cobalt ferrite, *J. Alloys Compd.* 617 (2014) 547–562 (n.d.).
- G. Mustafa, M.U. Islam, W. Zhang, Y. Jamil, A.W. Anwar, M. Hussain, M. Ahmad, Investigation of structural and magnetic properties of Ce^{3+} -substituted nanosized Co-Cr ferrites for a variety of applications, *J. Alloys Compd.* 618 (2015) 428–436 (n.d.).
- M. Stefanescu, M. Barbu, T. Vlase, P. Barvinschi, L. Barbu-Tudoran, M. Stoia, Novel low temperature synthesis method for nanocrystalline zinc and magnesium chromites, *Thermochim. Acta* 526 (2011) 130–136.
- E. Stefan, J.T.S. Irvine, Synthesis and characterization of chromium spinels as potential electrode support materials for intermediate temperature solid oxide fuel cells, *J. Mater. Sci.* 46 (22) (2011) 7191–7197 (n.d.).
- C.L. Honeybourne, R.K. Rasheed, Nitrogen dioxide and volatile sulfide sensing properties of copper, zinc and nickel chromite, *J. Mater. Chem.* 6 (1996) 277–283.
- Y. Yamasaki, T. Arima, Y. Tokura, Magnetic reversal of the ferroelectric polarization in a spinel-type $CoCr_2O_4$, *Kotai Butsuri* 42 (2007) 29–36.
- N.M. Khalil, M.B. Hassan, E.M.M. Ewais, F.A. Saleh, Sintering, mechanical and refractory properties of MA spinel prepared via co-precipitation and sol-gel techniques, *J. Alloys Compd.* 496 (2010) 600–607.
- M. Bayhan, T. Hashemi, A.W. Brinkman, Sintering and humidity-sensitive behaviour of the $ZnCr_2O_4$ - $K_2Cr_2O_4$ ceramic system, *J. Mater. Sci.* 32 (1997) 6619–6623.
- A.D. White, High Pressure Study of Spinel Chromite, PhD Thesis, 2005.
- T.D. Sparks, M.C. Kemei, P.T. Barton, R. Seshadri, E.-D. Mun, V.S. Zapf, Magnetocapacitance as a sensitive probe of magnetostructural changes in $NiCr_2O_4$, *Phys. Rev. B* 89 (2014), 024405.
- S.A. Bakar, N. Ahad, E.B. Saion, Thermal Treatment Synthesis and Characterization of Nanosized Nickel Chromite Spinel., *Solid State Science and Technology.* 21 (n. d.) 47–54.
- S. Klemme, J.C. Van Miltenburg, Thermodynamic properties of nickel chromite ($NiCr_2O_4$) based on adiabatic calorimetry at low temperatures, *Phys. Chem. Miner.* 29 (10) (2002) 663–667 (n.d.).
- F. Beshkar, M. Salavati-Niasari, Facile synthesis of nickel chromite nanostructures by hydrothermal route for photocatalytic degradation of acid black 1 under visible light, *J. Nanostruct.* 5 (2015) 17–23.
- Xiaoyang Xu, Jianping Gao, Wei Hong, Ni-based chromite spinel for high-performance supercapacitors, *RSC Adv.* 6 (35) (2016) 29646–29653 (n.d.).
- J.B. Goodenough, J.M. Lango, Landolt-Bornstein Tabellen, New Series, Vol. III/4a, Springer, Berlin, 1970.
- M. Nadeem, M.J. Akhtar, A.Y. Khan, Effects of low frequency near metal-insulator transition temperatures on polycrystalline $La_{0.65}Ca_{0.35}Mn_{1-y}Fe_yO_3$ (where $y=0.05$ – 0.10) ceramic oxides, *Solid State Commun.* 134 (2005) 431–436.
- A. Rathi, P.D. Babu, P.K. Rout, V.P.S. Awana, V.K. Tripathi, R. Nagarajan, B. Sivaiah, R.P. Pant, G.A. Basheed, Anomalous nano-magnetic effects in non-collinear spinel chromite $NiCr_2O_4$, *J. Magn. Magn. Mater.* 474 (2019) 585–590.
- A. Yousef, R. Tali, Preparation and Characterization of Spinel $NiCr_2O_4$ by Co-precipitation Method, (n.d.).
- S. Ghosh, A.D. Sharma, R.N. Basu, H.S. Maiti, Influence of B site Substituents on Lanthanum Calcium Chromite Nanocrystalline Materials for a Solid-Oxide Fuel Cell, *J. Am. Ceram. Soc.* 90 (2007) 3741–3747.
- A. Sutka, G. Mezinskas, Sol-gel auto-combustion synthesis of spinel-type ferrite nanomaterials, *Front. Mater. Sci.* 6 (2012) 128–141.
- J. Rodriguez-Carvajal, FULLPROF: a program for Rietveld refinement and pattern matching analysis, in: Abstracts of the Satellite Meeting on Powder Diffraction of the XV Congress of the IUCr, Toulouse, France, 1990, p. 127 (n.d.).
- B.R. Rehani, P.B. Joshi, K.N. Lad, A. Pratap, Crystallite Size Estimation of Elemental and Composite Silver Nano-powders Using XRD Principles, 2006.
- V.D. Mote, Y. Purushotham, B.N. Dole, Williamson-Hall analysis in estimation of lattice strain in nanometer-sized ZnO particles, *J. Theor. Appl. Phys.* 6 (1) (2012), 6., (n.d.).
- R. Nongjai, S. Khan, K. Asokan, H. Ahmed, I. Khan, Magnetic and electrical properties of In doped cobalt ferrite nanoparticles, *J. Appl. Phys.* 112 (2012), 084321.
- H.S.C. O'Neil, A. Navrotsky, Cation distributions and thermodynamic properties of binary spinel solid solutions, *Am. Mineral.* 69 (1984) 733–753.
- M.A. Kassem, A.A. El-Fadl, A.M. Nashaat, H. Nakamura, Structure, optical and varying magnetic properties of insulating MCo_2O_4 ($M=Co, Zn, Mg$ and Cd) nanospinel, *J. Alloys Compd.* 790 (2019) 853–862.
- M. Akyol, İ. Adanur, A.O. Ayaş, A. Ekicibil, Magnetic field dependence of magnetic coupling in $CoCr_2O_4$ nanoparticles, *Physica B Condens. Matter* 525 (2017) 144–148.
- J.K. Burdett, G.D. Price, S.L. Price, Role of the crystal-field theory in determining the structures of spinels, *J. Am. Chem. Soc.* 104 (1982) 92–95.
- S.G. Prabhulkar, R.M. Patil, Nanosized Nickel doped Copper Chromite Spinel Particles: Synthesis, Characterization and Photocatalytic Applications, *Res. J. Mater. Sci.* 1 (October(9)) (2013) 1–9 (n.d.).
- J.R. Macdonald, Impedance Spectroscopy—Emphasizing Solid Materials and Systems, Wiley-Interscience, John Wiley and Sons, 1987, pp. 1–346.
- M.M. Costa, G.F.M. Pires Jr., A.J. Terezo, M.P.F. Graca, A.S.B. Sombra, Impedance and modulus studies of magnetic ceramic oxide $Ba_2Co_2Fe_{12}O_{22}$ (Co_2Y) doped with Bi_2O_3 , *J. Appl. Phys.* 110 (2011), 034107.
- M. Ahmad, M.A. Rafiq, Z. Imran, K. Rasool, R.N. Shahid, Y. Javed, M.M. Hasan, Charge conduction and relaxation in MoS_2 nanoflakes synthesized by simple solid state reaction, *J. Appl. Phys.* 114 (2013), 043710.
- H. Rahmouni, M. Nouri, R. Jemai, N. Kallel, F. Rzigua, A. Selmi, K. Khirouni, S. Alaya, Electrical conductivity and complex impedance analysis of 20% Ti-doped $La_{0.7}Sr_{0.3}MnO_3$ perovskite, *J. Magn. Magn. Mater.* 316 (2007) 23–28.
- M. Ahmad, M.A. Rafiq, M.M. Hasan, Transport characteristics and colossal dielectric response of cadmium sulfide nanoparticles, *J. Appl. Phys.* 114 (2013), 133702.
- L.B. Schein, D. Glatz, J.C. Scott, Observation of the transition from adiabatic to nonadiabatic small polaron hopping in a molecularly doped polymer, *Phys. Rev. Lett.* 65 (1990) 472.
- S. Kominé, E. Iguchi, Dielectric properties in $LaFe_{0.5}Ga_{0.5}O_3$, *J. Phys. Chem. Solids* 68 (8) (2007) 1504–1507 (n.d.).
- Z. Lu, J. Zhu, E. Andrew Payzant, M.P. Paranthaman, Electrical conductivity of the manganese chromite spinel solid solution, *J. Am. Ceram. Soc.* 88 (2005) 1050–1053.
- S.S. Ata-Allah, F.M. Sayedahmed, M. Kaiser, A.M. Hashhash, Crystallographic and low frequency conductivity studies of the spinel systems $CuFe_2O_4$ and $Cu_{1-x}Zn_xGa_{0.1}Fe_{1.9}O_4$ ($0.0 \leq x \leq 0.5$), *J. Mater. Sci.* 40 (2005) 2923–2930.
- M. Megdiche, C. Perrin-Pellegrino, M. Gargouri, Conduction mechanism study by overlapping large-polaron tunnelling model in $SrNiP_2O_7$ ceramic compound, *J. Alloys Compd.* 584 (2014) 209–215.
- E.V. Gopalan, P.A. Joy, I.A. Al-Omari, D.S. Kumar, Y. Yoshida, M. R. Anantharaman, On the structural, magnetic and electrical properties of sol-gel derived nanosized cobalt ferrite, *J. Alloys Compd.* 485 (2009) 711–717.
- A.K. Jonscher, The 'universal' dielectric response, *Nature* 267 (1977) 673.
- M. Prabu, S. Selvasekarapandian, Dielectric and modulus studies of $LiNiPO_4$, *Mater. Chem. Phys.* 134 (2012) 366–370.
- A. Dutta, T.P. Sinha, P. Jena, S. Adak, Ac conductivity and dielectric relaxation in ionically conducting soda-lime-silicate glasses, *J. Non-Cryst. Solids* 354 (2008) 3952–3957.
- J.M. Reau, S. Rossignol, B. Tanguy, J.M. Rojo, P. Herrero, R.M. Rojas, J. Sanz, Conductivity relaxation parameters of some Ag+ conducting tellurite glasses containing AgI or the (AgI) 0.75 (TlI) 0.25 eutectic mixture, *Solid State Ion.* 74 (1994) 65–73.

- [46] Ankurava Sinha, Abhigyan Dutta, Microstructure evolution, dielectric relaxation and scaling behavior of Dy-for-Fe substituted Ni-nanoferrites, RSC Adv. 5 (121) (2015) 100330–100338 (n.d.).
- [47] A.M. Farid, A.E. Bekheet, AC conductivity and dielectric properties of Sb₂S₃ films, Vacuum 59 (2000) 932–939.
- [48] T.G. Reddy, B.R. Kumar, T.S. Rao, J.A. Ahmad, Structural and dielectric properties of barium bismuth titanate (BaBi₄Ti₄O₁₅) ceramics, Int. J. Appl. Eng. Res. Dev. 6 (2011) 571–580.